Quantifying the Heat Load to Conductors Due to Strain Energy Release in CTD-101 K Magnet Impregnant

Jan van Steenlandt, Anna Kario, Simon Otten, Laurent Warnet, Sander Wessel, Herman ten Kate, and Hans van Oort

***Abstract*—State-of-the-art Nb_3Sn superconducting accelerator magnets are still prone to lengthy training. This study investigates whether direct heat from fractures in commonly used magnet impregnant is sufficient to cause the instabilities during training. To do so, the strain energy release rate of CTD-101 K epoxy is measured in liquid nitrogen at 77 K, together with the temperature of a nearby copper element representing a Nb_3Sn strand in the magnet windings. This experiment provides evidence that a large part of the mechanical energy is converted into heat. An analytical model using strain energy release rate data of impregnates at 4.2 K shows that this heat can contribute to the first quenches during magnet training.**

***Index Terms*—CTD-101 K, impregnant, magnet, Nb_3Sn, strain energy release rate, training.**

I. Introduction

TODAY, long training is still present in various types of Nb_3Sn superconducting accelerator magnets such as those for HL-LHC [1]. Training is defined as a progressive improvement in performance after repeated quenching [2]. Each premature quench during training is time and resource consuming [3]. In this study, we contribute to the understanding of the origin of these premature quenches in order to limit their amount.

Training can be due to fractures of the magnet impregnant, which is usually epoxy resin for accelerator magnets [4]. Some evidence is provided by the BOnding eXperiment (BOX) on Nb_3Sn cable, which demonstrates that the type of impregnation material directly affects the length of training and can even eliminate it when using a different impregnant than epoxy, such as paraffin [5]. Paraffin was already used as impregnant in the 1970s [6]. Hence, this material is currently being applied in a training-free racetrack Nb_3Sn coil termed BigBOX [7]. Other evidence is from sub-scale epoxy impregnated Nb_3Sn magnets, where measurements with acoustic sensors [8], strain gauges [9], and rotating pick-up coils [10] indicate epoxy cracking during training.

The finite element model of Vallone et al. [11] aimed to reproduce such measurement data by using cohesive zone elements at the expected crack locations, mainly at the interface with the magnet support structure. By also reproducing the training curve of these magnets, this model shows that direct heat from these cracks is a sufficiently strong thermal disturbance to explain mainly the initial steep part of the training curve. However, this model relies on many unverified assumptions about the conversion of strain energy into heat.

In the 1980s, several authors have studied heat release during epoxy fracture at 4.2 K [12], [13], [14], [15], [16]. Different specimen types were used, but all measured temperature increase with Au or Ag – chromel thermocouples. This article is a contribution to this line of work by using CTD-101 K epoxy resin and by relating temperature rise for the first time to the strain energy release rate, a commonly used material property assumed to govern the process. Furthermore, this property has been measured often at cryogenic temperatures with standardized experiments and can thus be verified easily [17], [18], [19].

The first goal of this study is to obtain experimental data on both the strain energy release rate and the heat generated by a fracture within CTD-101 K epoxy, a common magnet impregnate. However, this study is limited to fractures in the bulk of the epoxy at a temperature of 77 K and a mode I load case, i.e., a load applied normal to the crack plane.

The second goal of this study is to use strain energy release rate data at 4.2 K and model the occurrence of premature training quenches. This relatively simple analytical model is applied to the BOX experiment for its relative simplicity compared to a full magnet.

II. Experiment to Measure the Heat Generated During Fracture

The strain energy release and heat generated by the emergence of a crack are obtained using a modified mode I compact tension double cantilever beam (CT-DCB) specimen of CTD-101 K. The modification is achieved by embedding a copper tube with a braided fiberglass sleeve in the center of the crack plane along the direction of the crack. It represents a Nb_3Sn strand in the vicinity of the crack. The change in temperature of this copper tube allows to determine the heat generated. The specimen is tested

Received 5 March 2025; revised 14 May 2025; accepted 20 May 2025. Date of publication 6 June 2025; date of current version 17 June 2025. *(Corresponding author: Anna Kario.)*

The authors are with the University of Twente, 7522 NB Enschede, The Netherlands (e-mail: anna.kario@cern.ch).

Color versions of one or more figures in this article are available at https://doi.org/10.1109/TASC.2025.3573388.

Digital Object Identifier 10.1109/TASC.2025.3573388

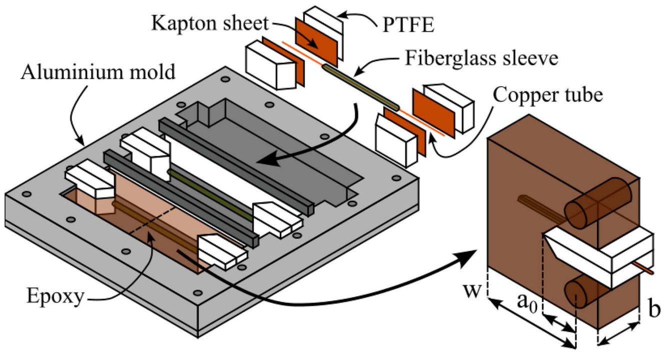

Fig. 1. Specimen preparation method.

at 77 K while submerged in liquid nitrogen at 1 atm ambient pressure using a custom-made cryogenic stress–strain setup.

A. Specimen Preparation

To replicate the surface conditions of a Nb_3Sn strand in a cable, the copper tube is first ultrasonically cleaned and then briefly submerged in V4BR, a typical nafta petroleum based cabling lubricant [20]. The tube of 0.85 mm outer diameter and 0.4 mm inner diameter is inserted in a S2-type fiberglass sleeve made to fit the outer tube diameter. Both are subjected to a short heat treatment of 1 h at 665 °C in a pure Argon atmosphere at around 6 mbar overpressure. This ensures the burned organic material of the braid is deposited on the copper surface as is the case during heat treatment of Nb_3Sn coils.

Fig. 1 shows schematically how the specimens are further prepared.

First, as shown on Fig. 1, the ends of the copper tube are glued with cyanoacrylate between two 25-µm-thick Kapton sheets and clamped between two 3-mm-thick blocks of polytetrafluoroethylene (PTFE). Then, the surfaces of the Kapton sheet exposed to epoxy are coated with QZ13 mold release agent. The assembly is placed in slots of a PTFE coated aluminium mold. This will ensure that the Kapton sheets form a 50-µm-wide notch serving as crack starter.

Further, the CTD-101 K epoxy is prepared according to the manufacturer specifications. After mixing and degassing, the epoxy is poured into the mold and cured at 110 °C for 5 h and 125 °C for 16 h.

Last, the casts of two specimens are further split using a water cooled diamond coated saw and pin-holes are made using a CNC drill. In the end, each specimen resembles a CT-DCB specimen from the linear elastic fracture mechanics (LEFM) standard for plastics [22]. This is mainly to ensure plane strain conditions. The specimen dimensions are indicated on Fig. 1. For the two specimens reported in this article, the values are listed in Table I.

B. Setup and Measurement Procedure

In Fig. 2, the cryogenic stress–strain setup is schematically explained.

TABLE I
SPECIMEN DIMENSIONS. ACCURACY $\pm 1\,\alpha$

Name of dimension	Symbol	Specimen	Value [mm]
Initial crack length	a_0	1	21.3 ± 0.1
		2	21.66 ± 0.05
Thickness	b	1	18.60 ± 0.02
		2	18.01 ± 0.02
Arm length	w	1 & 2	40

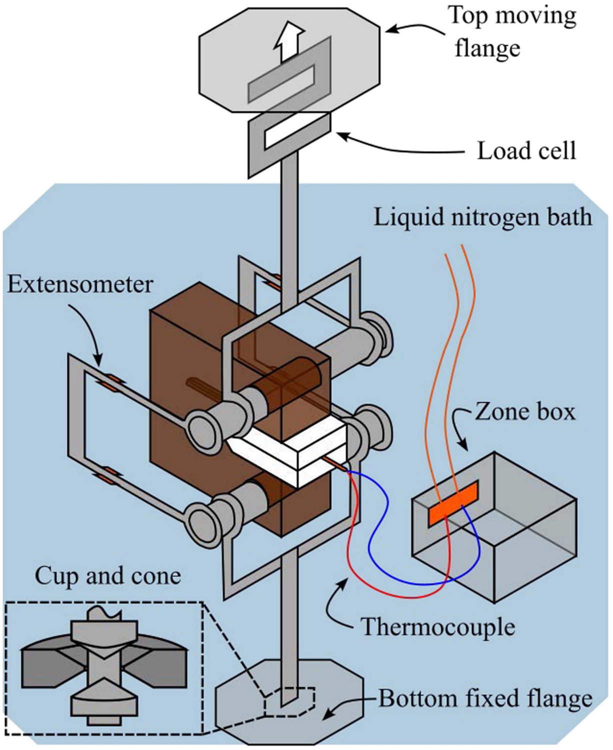

Fig. 2. Cryogenic stress-strain setup and instrumentation.

A moveable top flange is connected to an S-shaped load cell (Tedea Huntleigh model 615 500 kg). The load cell was calibrated using a device calibrated by NMi, reaching an accuracy of 3 N. From this load cell, a 1-m-long rod extends down into a cryostat containing liquid nitrogen. This rod connects to the top pin of the CT specimen.

The displacement is measured with two custom-made extensometers connected to the ends of the top and bottom pins. They have been calibrated in liquid nitrogen by using the setup without specimen and measuring the displacement of the top flange with a digital micrometer, reaching an accuracy of 17 µm.

The temperature is measured using a thermocouple having a composition similar to type E (Goodfellow, 0.125 mm, 80w% Ni, 20w% Cr Chromel and 55w% Cu, 45w% Ni Constantan). The zone box of aluminium is also submerged in liquid nitrogen at the same level as the specimen [21]. The thermocouple is calibrated in the vicinity of 77 K with a calibrated CERNOX sensor to obtain a linearized coefficient of 57400 ± 400K/V. With an amplification of 1000, an accuracy of ± 3 mK is achieved.

To prevent tensile thermal stresses and associated cracks during cooldown, a cup and cone connection is made between the bottom fixed flange and the specimen rod. This is shown in the inset in Fig. 2.

The specimen is first compressed by moving the top flange down. This prevents tensile stresses in the specimen during cooldown. Then, the specimen is slowly cooled down by cold nitrogen gas to around 150 K in order to avoid fracture by thermal shock. Next, after submerging in liquid nitrogen at 77 K and waiting for 1 h, the top flange together with the top pin are moved up at a relatively low speed of 1 µm/s.

If a fracture event occurs, the displacement is stopped several seconds later. The specimen is then unloaded to zero load and reloaded several times until no stiffness is noted.

In addition, the load–displacement of a setup compliance correction specimen is measured. This sample is prepared with the same procedure, but without PTFE blocks or Kapton crack starter. The same pin-hole clearance and surface condition is ensured for matching pin indentation. Also, the same measurement setup and conditions are applied and several ramps were done between 0 and 2000 N.

C. Data Analysis

1) Mechanical Strain Energy Release Rate: First, for each load cycle having index i, the measured load and displacement are linear least square fitted to obtain a slope S_i^* in units of N/m. This fit is performed between 25% and 95% of the maximum load achieved just prior to the fracture event, hereby noted as $\bar{F}_i$.

Second, the slope is corrected with that of the setup compliance correction specimen S_c by subtracting its displacement at similar load. This is also suggested in the LEFM standard for plastics [22]. This can be summarized as

$$S_i = \left(\frac{1}{S_i^*} - \frac{1}{S_c}\right)^{-1} \quad \text{[N/m]}. \tag{1}$$

Equation (1) causes on average a 25% correction on the slope for the first loading cycle.

Third, the strain energy released during each load cycle W_i is obtained as the area between the load–displacement curves of load cycle i and that of cycle $i+1$, both up to $\bar{F}_i$

$$W_i = \frac{\bar{F}_i^2}{2S_i}\left(1 - \frac{S_{i+1}}{S_i}\right) \quad \text{[J]}. \tag{2}$$

Next, the crack length during each load cycle is estimated using the compliance method. To do so, the specimen plane strain modulus is first calculated from the slope of the initial or 0th ramp S_0. This is done with numerically obtained functions $f(\alpha)$ and $\phi(\alpha)$, where α is the crack length a relative to the arm length of the specimen w (40 mm). Both symbols are indicated on Fig. 1. $f(\alpha)$ and $\phi(\alpha)$ are listed for CT-DCB specimens in the LEFM standard for plastics, where the following formula can also be found [22]:

$$E = \frac{2\, f(\alpha_0)^2\, \phi(\alpha_0)\, S_0}{w} \quad \text{[Pa]}. \tag{3}$$

As input, α_0 is obtained by measuring $(w - a_0)$ five times on the fractured surfaces after the test is finished. This is done using a Leica S9D microscope, an sCMEX-6 camera and calibrated digital image analysis software. For the two specimens reported here, (3) gives: $E = 6.9 \pm 0.2$ GPa and 6.8 ± 0.2 GPa. These values are only slightly higher than 6.6GPa, which is the value obtained by Brem et al. (2021) for CTD-101K, using dynamic mechanical thermal analysis (DMTA) at around 150 K and corrected for plane strain using $\nu = 0.3$ [18].

The crack length for further load cycles then follows from (3) by equating E for each load cycle. α_i is then obtained through interpolation of $f(\alpha_i)^2\phi(\alpha_i)$. This can be summarized as

$$f(\alpha_i)^2\, \phi(\alpha_i) = f(\alpha_0)^2\, \phi(\alpha_0)\, \frac{S_0}{S_i} \quad \text{[-]}. \tag{4}$$

Last, the strain energy release rate for each load cycle G_i follows from the released strain energy W_i in (2) and the relative crack length α_i in (4). As further input, the thickness of the specimen b (18 mm) is measured as indicated in Fig. 1. The calculation below uses the formula with calibration factor from the same standard for plastics [22]. However, crack arrest is observed in this experiment, meaning that the reduction in load appears to stabilize the crack and stop it within the sample, instead of the crack continuing in an unstable manner. This is not accounted for in the ISO standard. Hence, an approximation is made by evaluating ϕ and S at the average of subsequent load cycles

$$G = \frac{-1}{b\,w}\,\frac{dW}{dS}\,\frac{S}{\phi(\alpha)} \tag{5}$$

$$G_i \approx \frac{-1}{b\,w}\,\frac{W_i}{S_{i+1} - S_i}\,\frac{(S_i + S_{i+1})/2}{\phi((\alpha_i + \alpha_{i+1})/2)} \quad [\mathrm{J/m^2}]. \tag{6}$$

2) Thermal Heat Load: The measured temperature as function of time for each load cycle is fitted with an exponential function using linear least squares. This fit is made within a period starting two seconds after the occurrence of the fracture, up to the moment of unloading. Also, the data recorded in the period that the motor is stopped are excluded from the fit, as will be explained later.

This fit allows to obtain coefficients A_i and τ_i. The temperature rise caused by the fracture ΔT_i is then extrapolated using this fit to the time of fracture t_f using

$$\Delta T_i = A_i e^{-t_f/\tau_i} \quad \text{[K]}. \tag{7}$$

The time of fracture t_f itself is measured as the moment that the reading of the load cell drops.

The fit above assumes that the copper tube behaves as a lumped capacity when cooling down. This can be checked with the Biot number $Bi = \bar{h}L/\kappa$. For boiling nitrogen, a convection correlation valid up to a difference of 10 K is $\bar{h} = 5 \cdot 10^2\,(\Delta T)^{1.5}\ \mathrm{W/m^2\,K^{2.5}}$ [23]. The length of the tube L is 58 mm. The conductivity of copper is estimated as 506 W/mK at 78 K. This assumes a poor residual resistance ratio (RRR) of 50 in the NIST fit listed in [24]. With these values, for a temperature increase of 1 K, $Bi = 6 \cdot 10^{-2}$, which is slightly below 0.1. Hence, given the use of poor conductivity in this

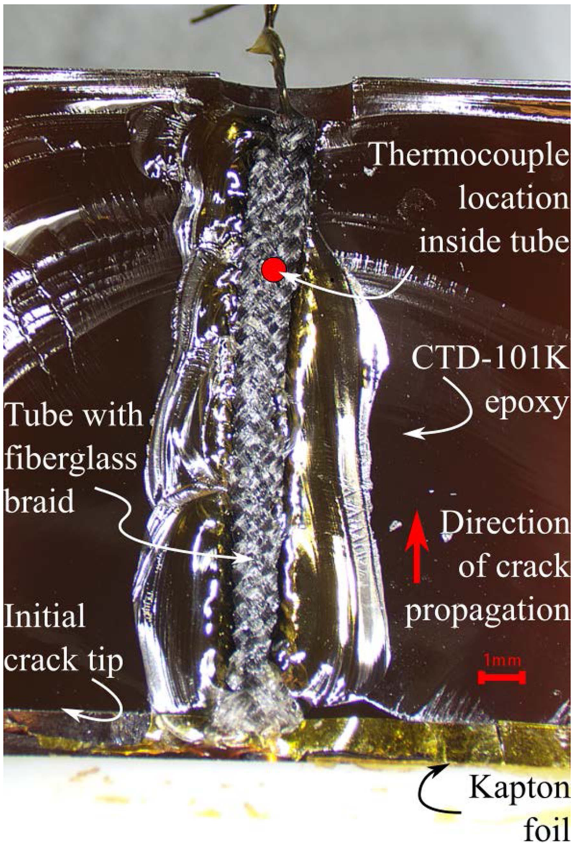

Fig. 3. Picture of the fractured surface of specimen 1 with annotations for the parts and the principal direction of crack propagation.

estimate and that the actual measured temperature increase is below 1 K, the assumption of a lumped capacity is likely valid.

Next, the heat load received by the copper tube can be obtained using ΔT_i from (7). First, if the heat deposition is assumed to be adiabatic, the thermal energy received is the product of the heat capacity of the copper ρc_p and its volume V. Then, if the heat load is assumed to be uniformly deposited, the thermal energy can be divided by the surface receiving the heat. This surface can be approximated as the product of the crack propagation length and the circumference of the tube receiving the heat d^* . This is taken as the average between the tube outer diameter (0.85 mm) and half its circumference. Hence, the heat load is given by

$$E_i^{\mathrm{th}} = \frac{\rho c_p \Delta T_i V}{d^* w\left(\alpha_{i+1} - \alpha_i\right)} \quad [\mathrm{J/m^2}]. \tag{8}$$

Equation (8) uses the density and specific heat of copper at 77 K: $\rho = 8960$ kg/m^2 and $c_p = 195$ J/kg K [24]. The volume of the tube V is 26 mm^3.

D. Results and Discussion

An image of the cracked surface of specimen 1 is shown in Fig. 3. On this picture can be seen that multiple crack arrest lines are present that are not straight. Several features are parallel along the length of the strand.

Fig. 4 shows the load displacement curves of specimen 1 during subsequent cycles. The data during unloading is left out for clarity. Also, the data plotted is that after performing the setup compliance correction.

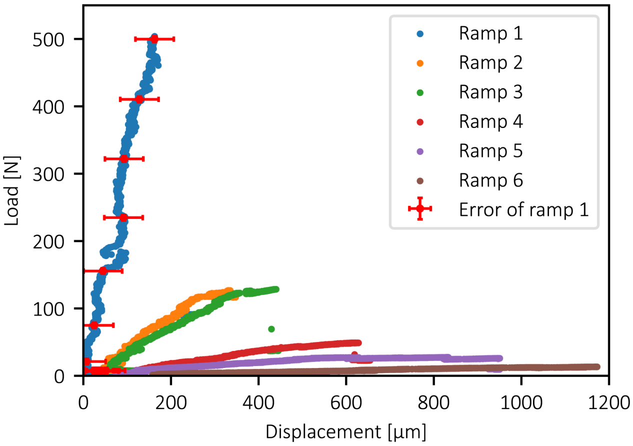

Fig. 4. Measured load displacement curves for specimen 1. Accuracy ± 1 α.

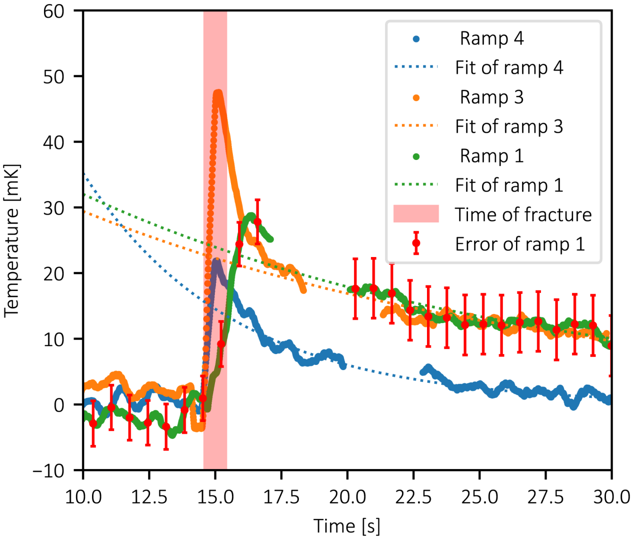

Fig. 5. Measured temperature increase versus time during fractures for specimen 1. Accuracy ± 1 α.

In Fig. 4, it is further demonstrated how crack arrest results in load cycles with decreasing slope, hence with increasing crack length. For specimen 1, most of the mechanical energy is released during the first and third fracture, the same fractures for which also a significant temperature increase is recorded.

In Fig. 5, the recorded temperature as function of time is indicated for several ramps to fracture for specimen 1. Only the temperature during ramps 1, 3, and 4 rises above the measurement accuracy. Other ramps showed no significant response. It can be seen that sections of 3 s in the data are removed. The data in these sections shows a sudden 20 mK change in offset at the exact moment when stopping the motor. The subsequent temperature data is corrected with this offset and found to continue the prior exponential decay. This change in offset is likely caused by a grounding error and not a thermo-elastic effect, since the offset is observed to be instantaneous and independent of ramp rate.

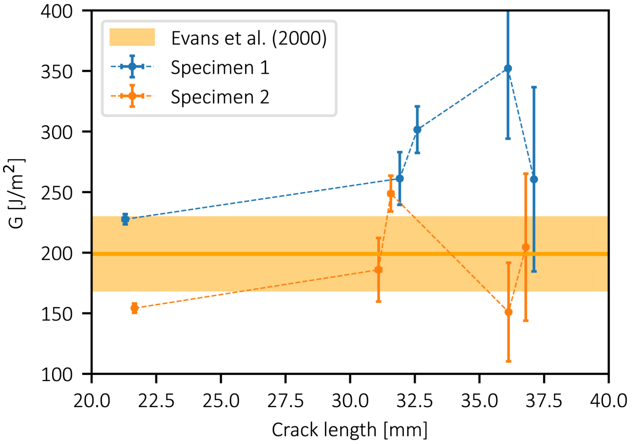

Fig. 6. Measured strain energy release rate as function of crack length for two specimens. Accuracy $\pm 1\,\alpha$.

In Fig. 5, it can be seen that a different temperature peak occurs prior to the exponential decay for ramps 1 and 3. This is believed to be due to the location of the thermocouple w.r.t. the crack tip. For specimen 1, the thermocouple is located at a location where the crack length is 35 mm (see Figs. 3 and 6). Hence, during ramp 3, the crack propagates nearer the thermocouple and produces a higher transient peak before the temperature in the tube is uniform.

Fig. 6 shows the measured strain energy release rate G as function of crack length for the two specimens with reproducible data. The dotted line shows the progression of the experiment. Combining all ten measured values on Fig. 6 leads to $G = 230 \pm 20$ J/m^2 (accuracy (spread) $\pm 1\,\alpha$). The bar in yellow indicates the value of $G = 199 \pm 30$ J/m^2 measured by Evans et al. [17] using single-edge-notched-bend specimens at 77 K tested at 3 µm/s. This data is for RAL-1, an anhydride cured DGEBA epoxy comparable to CTD-101K.

The curve in Fig. 6 should ideally be horizontal for a brittle material like epoxy at 77 K. Note that both specimens fluctuate around the literature value, but only two points for specimen 1, and three points for specimen 2, have overlapping error bars. The average value is also slightly higher. More specimens would be recommendable, but it is likely that the presence of the fiberglass and copper tube did not significantly affect the measured fracture property G compared to a specimen without this embedded element. However, the embedded element does seem to induce crack arrest and it creates the complex fracture surfaces in Fig. 3.

Last, Table II summarizes the obtained temperature rise at fracture given by (7), together with the corresponding surface heat load according to (8).

The value for E_{th} in Table II for ramp 1 and both specimens seems to match half the reported value of G. This provides evidence that approximately 100% of the mechanical energy is converted to a surface heat load on both fracture surfaces. It also means that on one surface, this energy is integrally transported to the copper tube. However, large errors of 30% are to be noted on E_{th} and values derived for later ramps are several times higher than expected.

TABLE II
MEASURED TEMPERATURE INCREASE AND SURFACE HEAT LOAD FOR TWO SPECIMENS. ACCURACY $\pm 1\,\alpha$

Specimen	Ramp	ΔT_f [mK]	E_{th} [J/m^2]
1	1	24 ± 5	90 ± 30
	3	22 ± 4	260 ± 80
	4	15 ± 4	600 ± 220
	2, 5, 6	≈ 0	≈ 0
2	1	24 ± 4	100 ± 30
	3	24 ± 5	220 ± 80
	2, 4, 5	≈ 0	≈ 0

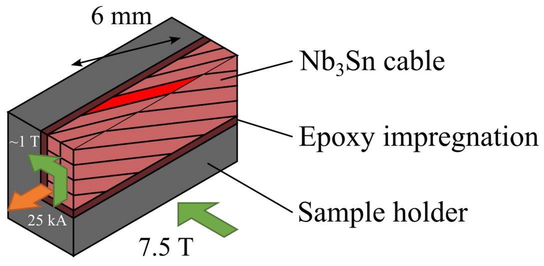

Fig. 7. BOX sample cutout. The strand with lowest margin modeled in this paper is marked in red. The Nb$_3$Sn cable is simplified with less strands for clarity.

This last observation can also be seen in Fig. 5, where roughly the same temperature increase occurs during ramps 1 and 3. However, in Fig. 6, it can be seen that the crack only extends half as far during ramp 3. The most likely explanation for this discrepancy is the assumption of a uniformly advancing crack front in (8). It is likely that during ramp 3, a larger strand area is being exposed than indicated by the average compliance based crack length.

Last, the zero entries in Table II concern ramps for which G could be measured, but no thermal heat load. This is because only small amounts of strain energy are released with minor crack advance. This energy converted to thermal energy could not be measured within the resolution of the thermocouples.

III. NB$_3$SN CABLE STABILITY MODEL FOR HEAT GENERATED DURING FRACTURES

We examine with a simple model whether premature quenches can be proven with the strain energy release rate of epoxies at 4.2 K, assuming the 100% conversion also holds at 4.2 K. The data for G by Evans is used, namely for RAL-1 (CTD-101K like epoxy) at 4.2K: 61 ± 6J/m^2 [17].

The model is applied to the BOX experiment. There, quench tests in a background magnetic field of around 7.5 T prove that similar training curves can be obtained as in CCT sub-scale coils [25]. Focus is put on a length of strand with the lowest margin, namely the strand located at the short edge where the cable self-field is reinforcing the background magnetic field. This is illustrated red in Fig. 7.

The minimum propagation zone (MPZ) is calculated for this critical section of strand when it is exposed to a heat load given by $G = 61 \pm 6$J/m^2. It further examines the initial quench currents measured in BOX samples with CTD-101K in Otten et al. (2022) [5]. The MPZ is checked if below the length of this critical strand in order to explain the occurrence of these quenches. This is summarized as

$$l_{\text{MPZ}} \leq \frac{tL_p}{N_s d_s} \quad [\text{m}]. \tag{9}$$

In this equation, t is the short width of the cable (1.475 mm), L_p is the twist pitch (70 mm), N_s is the number of strands (21), and d_s is the strand diameter (0.85 mm) [5], [25]. For BOX, this gives $l_{\text{MPZ}} \leq 5.8$ mm.

A. Model Description

By definition, a quench propagates in a length of strand given by the MPZ if it increased in temperature due to a disturbance and if the additional heat generated by current sharing can no longer be removed by thermal conduction. The derivation of the formula for the MPZ below can be found in Wilson [2]

$$l_{\text{MPZ}} = \sqrt{\frac{2k_{cu}}{\rho_{cu}} \frac{\lambda^2}{\left(I_q / \left(N_s A_s\right)\right)^2} \frac{T_{hs} - T_0}{\left(T_{hs} - T_{cs}\right) / \left(T_c^* - T_{cs}\right)}} \quad [\text{m}]. \tag{10}$$

$$\lambda = \frac{f_{cu/sc}}{1 + f_{cu/sc}} \quad [\text{-}]. \tag{11}$$

In this equation, the cable current just prior to quenching, I_q, is assumed equally distributed among N_s cable strands, each having a cross section A_s. Moreover, k_{cu} and ρ_{cu} are the thermal conductivity and electrical resistivity of the copper within the Nb$_3$Sn strands, respectively. $f_{cu/sc}$ is the volume ratio of Nb$_3$Sn to copper within the strands (1.2 ± 0.02) [25]. T_{cs} and T_c^* are the current sharing temperature and apparent critical temperature of the Nb$_3$Sn, respectively. These are explained further on.

Several steps are performed to evaluate (10). First, the background or operational temperature T_0 is 4.2 K. But, due to a fracture in the impregnant, the MPZ attains a "hot-spot" temperature given by T_{hs}. This temperature rise is calculated using the volume averaged superconductor and copper specific heat ρc_p and half the strain energy release rate G times the projected strand area used in previous sections $d^* = 1/2(1 + \pi/2)d_s$

$$\frac{1}{2} G d^* = A_s \int_{T_0}^{T_{hs}} \left(\left(1 - \lambda\right) \rho c_p|_{sc} + \lambda \rho c_p|_{cu}\right) dT \quad [\text{J/m}]. \tag{12}$$

Next, T_{cs} and T_c^* are obtained. To do so, the critical current density j_c of Nb$_3$Sn is needed as function of temperature. This should also be at the magnetic flux density B_s seen by the strand of interest. For this calculation, the scaling law used for the critical current density $j_c(B, T)$ is that of Godeke et al. without strain dependence [26]. The fitting parameters T_{c0}, B_{c20}, and C are obtained using nonlinear least square fitting of RRP strand I_c data found in [27, Fig. 3]. This data is assumed to have $\pm$ 3% error. The resulting fit parameters are listed in Table III.

TABLE III
Nb$_3$Sn SCALING LAW FIT PARAMETERS AND UNCERTAINTIES [27]

Fit parameter	Value
B_{c20}	27.8 ± 0.6 T
C	$1.11 \pm 0.03 \cdot 10^6$ AT^2
T_{c0}	16 ± 2 K

The total magnetic field B_s seen by the strand is calculated by iteratively evaluating the following equation (k is the iteration number):

$$B_s^k = B_0 + a j_c\left(B_s^{k-1}, T\right) N_s \left(1 - \lambda\right) A_s \quad [\text{T}]. \tag{13}$$

Here, $B_0 = 7.5$ T is the background magnetic field and $a = 52.7$ mT/kA is obtained analytically by approximating the cable as a rectangular conductor of size 1.475 × 9.85 mm^2 with a uniform density of line currents [25]. a then follows from the magnetic field in the middle of the rectangle's short edge, i.e. where the strand of interest is located.

At this point, the total cable critical current can be calculated

$$I_c = j_c(B_s, T_0) N_s \left(1 - \lambda\right) A_s \quad [\text{A}]. \tag{14}$$

This gives 25.0 kA at $B_0 = 7.5$ T and 16.8 kA when $B_0 = 10$ T. This is only 6% and 2% more than the average values measured on the CTD-101K BOX samples by Otten et al., respectively [5]. This small discrepancy is likely caused by assuming that the straight cable sections of BOX have no influence on each other when calculating a in (13).

Further, as explained earlier, the cable current just prior to quenching, I_q in (10), is set equal to 58 ± 1 % of this I_c at $B_0 = 7.5$ T [5].

With previous knowledge on j_c, T_{cs}, and T_c^* are obtained by performing a linear least square fit of $j_c(B_s, T)$ to obtain T_c^* at j_c=0 A/mm^2 and j_{c0}^* at T=0 K. By definition, T_{cs} is then given by [2]

$$T_{cs} = \left(T_0 - T_c^*\right) \frac{I_q / \left(N_s \left(1 - \lambda\right) A_s\right)}{j_{c0}^*} + T_c^* \quad [\text{K}]. \tag{15}$$

As a last step to evaluate (10), the properties of Nb$_3$Sn and copper: $\rho c_p|_{sc}$, $\rho c_p|_{cu}$, k_{cu} and ρ_{cu} are obtained at T_{hs} and B_s from NIST data in [24]. For the copper, a residual resistance ratio of 150 ± 50 is assumed [27].

Finally, taking all the previously listed uncertainties into account, (10) returns a value of $l_{\text{MPZ}} = 2.3 \pm 0.3$ mm. The inequality in (9) is thus valid and the occurrence of the quenches in BOX samples with CTD-101K can be explained with the heat from fractures within the impregnant.

B. Discussion

The model result has to be considered with care. A main issue is the likely occurrence of other sources of heat. Further, it should be noted that (10) is a first order approximation of the thermal diffusion equation. Lastly, there are also many assumptions of which most important are as follows.

1) There is still strain energy left in the impregnant after cracking during cooldown.
2) The heat is deposited adiabatically and no heat loss occurs besides conduction along the strand.

3) The complete cable quenches if only this single strand quenches, hence no current sharing between strands occurs.
4) The first training quench occurs at the strand with smallest margin indicated in red on Fig. 6.
5) The current is equally distributed between strands of the cable up until the quench, or when reaching the cable I_c.

This makes clear that direct evidence is needed from local measurements near the cable during training to check the assumptions and validate the result.

IV. CONCLUSION

The first part of this article showed with a mode I CT-DCB experiment at 77 K that the heat generated directly by a fracture within CTD-101 K epoxy impregnant can be experimentally measured. The total thermal energy received by a copper dummy Nb_3Sn strand is measured to be 95 ± 3 J/m^2. This seems to match with half the strain energy release rate G measured to be 230 ± 20 J/m^2. Hence evidence is found of (near) 100% conversion of the mechanical energy into thermal energy on fracture surfaces. However, reproducibility is limited to two samples. Nonetheless, the results show that the strain energy release rate is suitable to assess epoxy systems for impregnation of Nb_3Sn magnets.

The second part of the paper supports with a simple model whether this heat load is sufficient to initiate a quench in Nb_3Sn magnets. It uses literature data of G at 4.2 K and is applied to the Nb_3Sn cable samples in the BOX program. It predicts a minimum propagation zone of 2.3 mm, while 5.8 mm of strand could have been exposed to the heat from fractures. However, there are still many assumptions and more direct evidence is needed from local measurements near the cable during training to find if this process is really the largest contribution to magnet training.

ACKNOWLEDGMENT

The authors would like to thank members of the BOX program CERN HFM working group for support and discussing the results. The AI system ChatGPT was used to generate minor parts of the code to analyze the experimental data in the first part of this article.

REFERENCES

[1] E. Todesco et al., “The high luminosity LHC interaction region magnets towards series production,” *Supercond. Sci. Technol.*, vol. 34, 2021, Art. no. 053001.
[2] M. N. Wilson, *Superconducting Magnets*. Oxford, U.K.: Oxford Univ. Press, 1983.
[3] S. Stoynev et al., “Analysis of Nb_3Sn accelerator magnet training,” *IEEE Trans. Appl. Supercond.*, vol. 29, no. 5, Aug. 2019, Art. no. 4001206.
[4] Y. Iwasa, *Case Studies in Superconducting Magnets, Design and Operational Issues*, 2nd ed. Berlin, Germany: Springer, 2009.
[5] S. Otten et al., “Training curves of Nb_3Sn Rutherford cables with a wide range of impregnation materials measured in the BOX facility,” *IEEE Trans. Appl. Supercond.*, vol. 33, no. 5, Aug. 2023, Art. no. 4003605.
[6] P. F. Smith et al., “A solution to the ‘training’ problem in superconducting magnets,” *Cryogenics*, vol. 15, no. 4, pp. 201–207, Apr. 1975.
[7] D. M. Araujo et al., “Assessment of training performance, degradation and robustness of paraffin-wax impregnated Nb_3Sn demonstrator under high magnetic field,” *IEEE Trans. Appl. Supercond.*, vol. 34, no. 5, Aug. 2024, Art. no.7000208.
[8] M. Marchevsky, G. Sabbi, H. Bajas, and S. Gourlay, “Acoustic emission during quench training of superconducting accelerator magnets,” *Cryogenics*, vol. 69, pp. 50–57, 2015.
[9] J. L. R. Fernández et al., “Assembly and mechanical analysis of the canted-cosine-theta subscale magnets,” *IEEE Trans. Appl. Supercond.*, vol. 32, no. 6, Sep. 2022, Art. no. 4006505.
[10] S. I. Bermudez et al., “Performance of a MQXF Nb_3Sn quadrupole magnet under different stress level,” *IEEE Trans. Appl. Supercond.*, vol. 32, no. 6, Sep. 2022, Art. no.4007106.
[11] G. Vallone et al., “Modeling training in Nb_3Sn superconducting magnets,” *IEEE Trans. Appl. Supercond.*, vol. 34, no. 5, Aug. 2024, Art. no. 4903605.
[12] H. Maeda and Y. Iwasa, “Heat generation from epoxy cracks and bond failures,” *Cryogenics*, vol. 22, no. 9, pp. 473–476, Sep.. 1982.
[13] Y. Yasaka and Y. Iwasa, “Stress-induced epoxy cracking and energy release at 4.2 K in epoxy-coated superconducting wires,” *Cryogenics*, vol. 24, no. 8, pp. 423–428, Aug. 1984.
[14] O. Tsukamoto and Y. Iwasa, “Epoxy cracking in the epoxy-impregnated superconducting winding: Nonuniform dissipation of stress energy in a wire-epoxy matrix model,” *IEEE Trans. Magn.*, vol. MAG-21, no. 2, pp. 377–379, Mar. 1985.
[15] H. Yanagi et al., “Experimental study of energy release due to cracking of epoxy impregnated conductors,” *Cryogenics*, vol. 29, no. 7, pp. 753–757, Jul. 1989.
[16] S. Nishijima et al., “Effect of epoxy cracking on stability of impregnated windings related to thermal and mechanical properties,” in *Proc. Adv. Cryogenic Eng. Cryogenic Eng. Conf. Publ.*. Boston, MA, USA: Springer, 1988, vol. 33, pp. 125–133.
[17] D. Evans and Z. Zhang, “The work of fracture of epoxide resins at temperatures to 4K,” in *Advances in Cryogenic Engineering Materials*. Boston, MA, USA: Springer, 2000, pp. 235–242.
[18] A. Brem et al., “Elasticity, plasticity and fracture toughness at ambient and cryogenic temperatures of epoxy systems used for the impregnation of high-field superconducting magnets,” *Cryogenics*, vol. 115, Apr. 2021, Art. no. 103260.
[19] A. Gaarud et al., “Fracture toughness, radiation hardness, and processibility of polymers for superconducting magnets,” *Polymers (Basel)*, vol. 16, no. 9, May 2024, Art. no. 1287.
[20] A. Baskys, I. Pong, C. Sanabria, and E. M. Lee, “Image analysis capabilities and methodologies of Nb_3Sn Rutherford cables,” *IEEE Trans. Appl. Supercond.*, vol. 33, no. 5, Aug. 2023, Art. no. 4800606.
[21] G. Recktenwald, “Thermocouple.pdf, conversion of thermocouple voltage to temperature,” Portland State University, Portland, OR, USA, (n.d.). [Online]. Available: https://web.cecs.pdx.edu/gerry/epub/
[22] *Plastics — Determination of Fracture Toughness (GIC and KIC) — Linear Elastic Fracture Mechanics (LEFM) Approach*, ISO Standard 13586:2018, Second edition, 2018.
[23] J. W. Ekin, in *Experimental Techniques for Low-Temperature Measurements* (National Institute of Standards and Technology). Boulder, CO, USA: Oxford Univ. Press, 2006.
[24] G. Manfreda, “Numerical analysis of coupled thermal-electromagnetic problems in superconducting cables,” Ph.D. dissertation, Universita Degli Studi di Udine, Udine, Italy, 2007.
[25] M. Daly et al., “BOX: An efficient benchmark facility for the study and mitigation of interface-induced training in accelerator type high-field superconducting magnets,” *Supercond. Sci. Technol.*, vol. 34, 2021, Art. no. 115008.
[26] A. Godeke et al., “A general scaling relation for the critical current density in Nb_3Sn,” *Supercond. Sci. Technol.*, vol. 19, 2006, Art. no. R100.
[27] P. Ferracin et al., “The HL-LHC low-beta quadrupole magnet MQXF: From short models to long prototypes,” *IEEE Trans. Appl. Supercond.*, vol. 29, no. 5, Aug. 2019, Art. no. 4001309.